Nonlinear vibration of a sliding-mode-controlled structure: Simulation and experiment

Louis Mesny, Sébastien Baguet, Simon Chesné

Author manuscript, published in "Mechanical Systems and Signal Processing", Vol 211, 111209 (2024)
DOI: 10.1016/j.ymssp.2024.111209
The final publication is available at Elsevier via www.sciencedirect.com

Nonlinear vibration of a sliding-mode-controlled structure: simulation and experiment

L. Mesny[a], S. Baguet[a,*], S. Chesné[a]

[a]*INSA Lyon, CNRS, LaMCoS, UMR5259, 69621 Villeurbanne, France*

Abstract

In this paper, the combination of a nonlinear system and a robust sliding-mode controller with sliding integral surface is studied. This controller is composed of a linear part and a nonlinear part defined by a non-smooth function. Calculating the frequency response curve of such a system can be time-consuming and difficult using time integration methods. An original algorithm based on the harmonic balance method and capable of directly calculating the periodic solutions of a robust sliding-mode controller with sliding integral surface is proposed. In addition, the classical numerical methods for continuation of nonlinear frequency response curves and stability calculation of periodic solutions have been adapted to take into account the integral component of the control law. Finally, experimental validations on a non-linear structure have been carried out, attesting to the efficiency of the proposed controller and the robustness of the proposed numerical tools.

Keywords: Nonlinear dynamics, Active vibration control, Sliding mode control, Harmonic balance method

1. Introduction

In several industrial sectors, there is a growing emphasis placed on mitigating mechanical vibrations. Whether they are related to the aeronautics [1], automotive [2], or construction [3] sectors, they are the source of many hazardous problems for the system or for its user. Among all the existing strategies for reducing vibrations, two approaches stand out. The first approach involves a passive method with no external energy input, resulting in limited performance. The famous Tuned Mass Damper (TMD) is a notable example of this approach [4, 5]. However, the TMD is limited by its ability to damp a single frequency. The use of non-linear passive absorbers ensures frequency robustness [6]. Nevertheless, the management of bifurcation points, isolated solutions and changing stability becomes crucial in such cases [7]. The second approach is the active approach [8] which involves the integration of sensors, actuators, and control laws to enhance vibration damping. There is also a hybrid approach that combines both active and passive techniques. The hybrid approach ensures a "fail-safe" characteristic, whereby the passive component continues to dampen vibrations if the energy supply to the active component is disrupted [9, 10]. For the purpose of this paper, we focus on the active method.

The core component of active control [8] is the control law, responsible for regulating the energy flow between the active force and the information processed by the sensor. Selecting the appropriate control law is of paramount importance to achieve the desired behaviour. Numerous control laws have been developed in the literature, and in this study, sliding mode control (SMC) is adopted. SMC, initially designed for variable structures [11], stands out due to its robustness against disturbances, its applicability to non-linear systems, and its straightforward implementation [12, 13]. SMCs are essentially low-frequency controls for robotics, but some have provided excellent results in modal control, such as in the work of Zuo et al. [14] and more recently the paper of Rodriguez et. al. [15]. The main idea behind this control law is to drive the system dynamics on a predetermined regime such as a fixed point or a limit cycle [13]. This control is performed by a sliding manifold (sliding surface) that corresponds to a linear or nonlinear

*Corresponding author.
Email address: sebastien.baguet@insa-lyon.fr (S. Baguet)

combination of state variables (tracking error vector). The sliding mode control law is composed of two parts. A continuous part maintains the dynamics of the system on the sliding manifold and a non-smooth part (non-linear part) is constructed with a signum function that oscillates around the sliding manifold. The non-smooth nature of the control law represents a significant challenge when it comes to calculating the frequency response function. Readers who want more details about nonlinear systems with SMC and the use of the associated tools can refer to [16, 17].

The coupling between nonlinear dynamics and active control has received little attention in the literature. In the present paper, an original algorithm for calculating the frequency response curve of a nonlinear system under sliding mode control is proposed. For this purpose, the harmonic balance method [18] is combined with continuation and stability methods. However, because of the use of a sliding surface integral with a non-smooth control law, standard continuation and stability methods require several modifications.

The structure of this document is as follows. The operating system is described in section 2. The sliding mode control method and the harmonic balance method associated with the proposed algorithm are discussed in Sections 3 and 4. Sections 5 and 6 present the experimental study of a one-degree-of-freedom (DOF) nonlinear system and the experimental validation of the proposed algorithm. Finally, conclusions and perspectives are presented in Section 7.

2. System under consideration : nonlinear single-DOF reduced order model

A reduced order model of the nonlinear structure presented in Section 5 is considered. It is obtained through a modal projection on the first mode and therefore contains all the interesting dynamics in the vicinity of the first resonance. The resulting equation of motion taking active control into account reads:

$$M\ddot{x}(t) + C\dot{x}(t) + Kx(t) + f_{nl}(x) = f_{ext} + f_a(t) \tag{1}$$

with

$$f_{nl}(x) = K_{nl}x(t)^3 \tag{2}$$

$$f_{ext} = F\cos(\omega t) \tag{3}$$

In the context of this study, let us define the displacement as x(t), where M, C, K, and $K_{nl} \in \mathbb{R}^1$ represent the mass, damping, stiffness, and nonlinear stiffness of the system, respectively. For the harmonic perturbation f_{ext}, the amplitude and angular frequency are denoted as F and ω, respectively. The active component $F_a(t)$ will be discussed in detail in the following section. A visual depiction of the entire system is presented in Fig. 1.

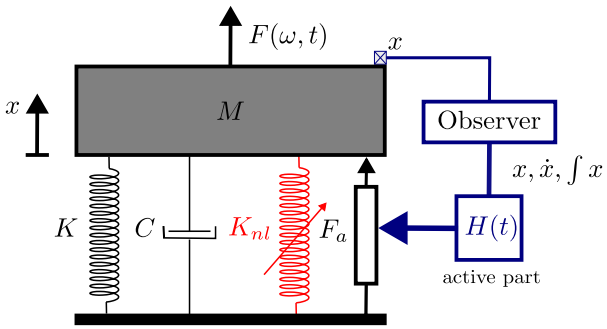

Figure 1: Diagram of the system studied.

3. Sliding mode control

The following section outlines the design of the sliding mode control method, which revolves around the utilization of a sliding manifold (also referred to as a sliding surface). The sliding manifold is devised to be a linear or nonlinear combination of the state vector.

Consider the tracking error of the oscillator position $x(t)$ as $e(t) = x(t) - x_d(t)$, where $x_d(t)$ represents the desired behaviour. In the context of vibratory applications, we assume that $x_d(t) = 0$, indicating that the desired behaviour of the system tends towards zero. The integral sliding manifold $\sigma(t)$ is defined by:

$$\sigma(t) = \alpha_1 x(t) + \alpha_2 \dot{x}(t) + \alpha_3 \int_0^t x(\tau) d\tau \tag{4}$$

with

$$\frac{\alpha_1}{\alpha_2} > 0 \text{ and } \frac{\alpha_3}{\alpha_2} > 0 \tag{5}$$

where $\int_0^t x(\tau)$ represents the integral of the structure's displacement. The benefit of an integral surface is to improve tracking performance and the speed of convergence of the method. [19, 20]. However, the integral term has very little influence on the dynamics of the steady-state regime. Fig. 2 illustrates the different phases of sliding mode control in the three-dimensional phase portrait. The initial stage, known as the reach phase, is aimed at bringing the system dynamics onto the sliding manifold. When the equation $\sigma(t) = 0$ is satisfied, it indicates that the system's dynamics are precisely on the sliding manifold. Subsequently, the sliding phase works towards aligning the system dynamics with the desired behaviour, such as limit cycles for the specific forced system under investigation. The sliding manifold plays a crucial role in the sliding mode control (SMC) approach as it governs the system's behaviour.

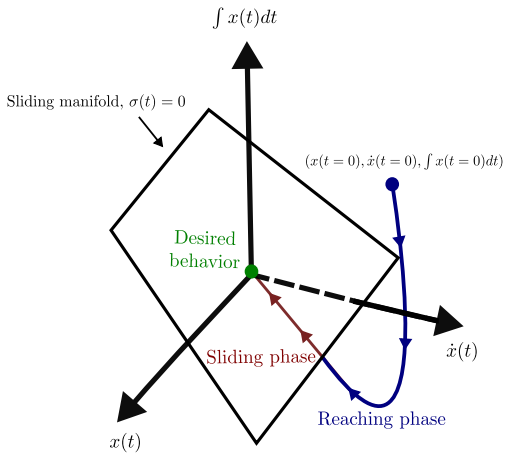

Figure 2: Phase portrait and diagram of different phases of SMC

3.1. Design of the sliding surface

The sliding manifold, represented by $\sigma(t)$, is formulated as a homogeneous differential equation. Consequently, Eq. (4) possesses a unique solution achieved when $\sigma(t) = 0$. Careful selection of the sliding manifold's parameters is necessary to ensure that the system dynamics presents the desired behaviour of asymptotically reaching zero (or the error $e(t) = x(t)$) with a well-designed controller. Various approaches exist for determining the optimal parameters of the sliding manifold, such as pole placement [21] or employing the method of linear quadratic minimization of cost function J. In this paper, the method of linear quadratic minimization is used to obtain the optimal parameters of the sliding manifold, as described below:

$$J = \frac{1}{2} \int_{t_s}^{+\infty} x^T Q x \, dt \tag{6}$$

with $x \in \mathbb{R}^{\mathbb{N}}$ being the state vector, $Q \in \mathbb{R}^{\mathbb{N}\times\mathbb{N}}$ both symmetric and positive definite weight matrixes, t_s the moment when the sliding mode starts, and $N = 3$, the numbers of necessary states. By minimizing the J function, the convergence of one state is prioritized over another, with the ultimate goal of swiftly attaining the desired behaviour.

Notably, the problem expressed in equation (6) is devoid of a penalty term, making it distinct from a conventional Linear-Quadratic Regulator (LQR), and can be considered a cost-free control problem. Following mathematical manipulations and transformations of Eq. (6), the parameters of the sliding surface (4) α_1, α_2, α_3 are obtained. These parameters ensure the finite-time convergence of the system's dynamics. The complete methodology of the linear quadratic minimization method is described extensively in [13].

3.2. Control law and understanding

To ensure the stability of the resulting system and the convergence of σ, the controller is designed by considering the Lyapunov function V and its derivative $\dot{V}$ [22]:

$$\begin{cases} V = \frac{1}{2}\sigma^2 \\ \dot{V} = \sigma\dot{\sigma} = \sigma(\alpha_1\dot{x}(t) + \alpha_2\ddot{x}(t) + \alpha_3 x(t)) \\ \dot{V} \leq -\nu|\sigma| \end{cases} \tag{7}$$

With :

$$\ddot{x}(t) = M^{-1}\left(-C\dot{x}(t) - Kx(t) - f_{nl}(x) + f_a(t)\right) = M^{-1}\left(-f\left(x, \dot{x}\right) + f_a(t)\right) \tag{8}$$

The convergence velocity of the trajectory to the sliding surface is determined by a strictly positive real constant, denoted ν [23]. Here, the sliding mode controller is specifically used to exhibit robustness against external disturbances. As a result, the controller is designed for the unforced system, where the external force is treated as an unknown disturbance that is periodic and bounded. V is chosen to satisfy the following conditions:

a) $\dot{V} < 0$ for $\sigma \neq 0$

b) $\lim_{|\sigma|\to+\infty} V = \infty$

From Eq.(7) and Eq.(8), assuming

$$\sigma(\alpha_1\dot{x}(t) + \alpha_2 M^{-1}\left(-f\left(x, \dot{x}\right) + f_a(t)\right) + \alpha_3 x(t)) \leq -\nu|\sigma| \tag{9}$$

The target condition is reached by the active force $f_a(t)$, as indicated:

$$f_a(t) = \left[-M\left(\frac{\alpha_3 x + \alpha_1\dot{x}}{\alpha_2}\right) + f\left(x, \dot{x}\right)\right] - \frac{M\nu}{\alpha_2} sign(\sigma(t)) = \eta(t) + f_{anl}(t) \tag{10}$$

with:

$$f\left(x, \dot{x}\right) = C\dot{x}(t) + Kx(t) + f_{nl}(x) \tag{11}$$

$$\eta(t) = -M\left(\frac{\alpha_3 x + \alpha_1\dot{x}}{\alpha_2}\right) + f\left(x, \dot{x}\right) \tag{12}$$

$$f_{anl}(t) = -\rho sign(\sigma(t)) \tag{13}$$

where $\rho = \frac{M\nu}{\alpha_2} > 0$ is the gain of the nonlinear active part and "sign" is the nonlinear signum function such that:

$$sign(\sigma) = \begin{cases} 1 & if\ \sigma(t) > 0 \\ 0 & if\ \sigma(t) = 0 \\ -1 & if\ \sigma(t) < 0 \end{cases} \tag{14}$$

The inclusion of a non-linear term containing the signum function in the system ensures stability in the Lyapunov sense of the linear component and contributes to the robustness of the overall system. The effectiveness of the control law relies on the level of non-smoothness exhibited by the active force. In this context, the signum function is considered to be theoretically the most efficient. However, due to practical considerations such as actuator longevity and the undesirable high-frequency harmonic generation known as the chattering effect [24], smoother versions of

this function are employed. These alternative versions include the saturation function, sigmoid function, and half-sinusoidal function, among others. Furthermore, in order to improve performance (reducing the maximum amplitude of the system within a specific frequency range), minimize control effort and reduce the chattering effect, it is common to weight the non-linear part of the sliding mode control law by the square root of the absolute value of the sliding surface, denoted as $\sqrt{|\sigma|}$:

$$f_a(t) = \eta(t) + \sqrt{|\sigma|} f_{anl}(t) \tag{15}$$

Finally, the full regularized system of equations of the considered system is:

$$\begin{cases} \Gamma(x, y, \omega, t) & = M\ddot{x}(t) + C\dot{x}(t) + Kx(t) + f_{nl}(x) - f_{ext} + f_a(x, y, t) \\ f_a(x, y, t) & = -M\left(\frac{\alpha_3 x + \alpha_1 \dot{x}}{\alpha_2}\right) + f(x, \dot{x}) - \rho\sqrt{|\sigma(t)|} \times \frac{\sigma(t)}{\sqrt{\sigma^2 + \epsilon}} \\ \sigma(x, y, t) & = \alpha_1 x(t) + \alpha_2 \dot{x}(t) + \alpha_3 y(t) \\ h(x, y, \omega, t) & = \dot{y}(t) - x(t) \end{cases} \tag{16}$$

where $\epsilon \ll 1$. In order to determine the amplitude of the steady-state regime at different frequencies, the system described by equation (16) can be solved using time integration for each frequency value within the specified range. The inclusion of the terms $\dot{y}(t) - x(t) = 0$ in equation (16) allows for the calculation of the integral term $\int_0^t x(\tau)d\tau$ and ensures the uniqueness of the solution. However, performing time integration becomes computationally demanding due to the extended duration of the transient response. To overcome this challenge, the next section presents a method based on the harmonic balance method, which enables the direct calculation of steady-state periodic solutions.

4. Harmonic balance algorithm for dynamic systems controlled by the sliding-mode method

Many methods can be used to calculate periodic solutions. Using the time-weighted residual method (orthogonal collocation method as in COCO [25], the shooting method, the global orbit search, the harmonic balance method, etc.). All these methods are explained in the review by Renson et al. [26].
For this section. 3, we describe the detailed algorithm for computing a frequency response function of a nonlinear system under a nonlinear control law. First, the harmonic balance method (HBM) is used. This method is based on the Fourier decomposition of periodic solutions [27]. Assuming $x(t)$ is a truncated periodic solution to the Fourier series of order H such that:

$$x(t) = a_0 + \sum_{k=1}^{H} a_k \cos(\omega k t) + b_k \sin(\omega k t) \tag{17}$$

where a_0, a_k and b_k are respectively constant, even and odd Fourier coefficients. Equation (17) is conveniently rewritten as:

$$x(t) = T_H(\omega t)X \tag{18}$$

with X the vector of Fourier coefficients and $T_H(\omega t) = [1 \;\; \cos(\omega t) \;\; \sin(\omega t) \;\; \ldots \;\; \cos(H\omega t) \;\; \sin(H\omega t)]$ of size $(2H + 1)$ the Fourier basis composed of trigonometric functions.
Introducing Eq. (18) in the first and last equations of (16) and applying a Galerkin procedure on $T_H(\omega t)$ [28] yields two equilibrium equations $R(X, Y, \omega)$ and $H(X, Y, \omega)$:

$$\begin{cases} R(X, Y, \omega) & = Z(\omega)X + F_{nl}(X) - P - F_a(X, Y, \omega) \\ H(X, Y, \omega) & = Y - \zeta(\omega)X \end{cases} \tag{19}$$

where

$$Z(\omega) = \omega^2 \nabla^2 M + \omega \nabla C + I_{(2H+1)}K \tag{20}$$

$$\zeta(\omega) = \frac{1}{\omega}\tilde{\nabla} \tag{21}$$

with M, C, K defined in Eq. (1) and where P, $F_{nl}(X, Y, \omega)$ are the vectors of Fourier coefficients of the external perturbation f_{ext}, the nonlinear forces f_{nl} and the active force $f_a(x, y, t)$ respectively. The term $I_{(2H+1)}$ is the identity

matrix of size $\mathbb{R}^{(2H+1)\times(2H+1)}$; ∇ is the derivative operator and $\tilde{\nabla}$ the integral operator which represent the pseudo-inverse of ∇ both dimensioned $\mathbb{R}^{(2H+1)\times(2H+1)}$ such that:

$$\nabla = diag(0, \nabla_1, \nabla_2, ..., \nabla_i, ..., \nabla_{\mathbf{H}}) \; with \; \nabla_i = i\begin{bmatrix} 0 & 1 \\ -1 & 0 \end{bmatrix} \tag{22}$$

$$\tilde{\nabla} = diag(0, \tilde{\nabla}_1, \tilde{\nabla}_2, ..., \tilde{\nabla}_2, ..., \tilde{\nabla}_H) \; with \; \tilde{\nabla}_i = \frac{1}{i}\begin{bmatrix} 0 & -1 \\ 1 & 0 \end{bmatrix} \tag{23}$$

The uniqueness condition, as previously explained in equation (16), is represented by the second equation of (19). The computation of the nonlinear forces $F_{nl}(X)$ and the active force $F_a(X, Y, \omega)$ will be formulated in section 4.1 and section 4.2 respectively. Furthermore, when constructing vector Y, care is taken to avoid introducing a rigid body mode through integration, as $\tilde{\nabla} \times \nabla$ does not yield a perfect identity matrix. More specifically, the first component contains a zero, which prevents the computation of the constant Fourier coefficient.

4.1. Computation of the nonlinear terms and their derivatives (AFT)

In order to deal with the non-linear term $f_{nl}(x, \dot{x})$ and bypass the need for convolution in the Fourier domain due to the time domain product, Cameron et al. [29] employed the AFT (Alternating Frequency Time) method. This approach utilizes the discrete Fourier transform to evaluate the non-linear term in the time domain, following which it returns to the Fourier domain, as illustrated in equation (24).

$$X \xrightarrow[DFT^{-1}]{} (x, \dot{x}) \longrightarrow f_{nl}(x, \dot{x}) \xrightarrow[DFT]{} F_{nl}(X) \tag{24}$$

The nonlinear forces $F_{nl}(X)$ and the general derivative terms $\frac{dF_{nl}(X)}{dX}$ are computed as follows [30]:

$$F_{nl}(X) = \Psi^{-1}\bar{f}_{nl}(x, \dot{x}) \tag{25}$$

$$\frac{dF_{nl}(X)}{dX} = \frac{\partial F_{nl}(X)}{\partial \bar{f}_{nl}}\frac{\partial \bar{f}_{nl}(X)}{\partial \bar{q}}\frac{\partial \bar{q}}{\partial Q} + \frac{\partial F_{nl}(X)}{\partial \bar{f}_{nl}}\frac{\partial \bar{f}_{nl}(X)}{\partial \dot{\bar{q}}}\frac{\partial \dot{\bar{q}}}{\partial Q} = \Psi^{-1}\frac{\partial \bar{f}_{nl}(x, \dot{x})}{\partial x}\Psi + \Psi^{-1}\frac{\partial \bar{f}_{nl}(x, \dot{x})}{\partial \dot{x}}\omega\Psi\nabla \tag{26}$$

with

$$\bar{f}_{nl}(x, \dot{x}) = \begin{bmatrix} f_{nl}(x(t_1), \dot{x}(t_1)) \\ f_{nl}(x(t_2), \dot{x}(t_2)) \\ \vdots \\ f_{nl}(x(t_N), \dot{x}(t_N)) \end{bmatrix} \tag{27}$$

$$\bar{x}(t) = \Psi X = \begin{bmatrix} x(t_1) \\ x(t_2) \\ \vdots \\ x(t_N) \end{bmatrix} \tag{28}$$

$$\dot{\bar{x}}(t) = \omega\Psi\nabla X = \begin{bmatrix} \dot{x}(t_1) \\ \dot{x}(t_2) \\ \vdots \\ \dot{x}(t_N) \end{bmatrix} \tag{29}$$

where

$$\Psi = \begin{bmatrix} 1 & \cos(\theta_1) & \sin(\theta_1) & \cdots & \cos(H\theta_1) & \sin(H\theta_1) \\ \vdots & \vdots & \vdots & & \vdots & \vdots \\ 1 & \cos(\theta_N) & \sin(\theta_N) & \cdots & \cos(H\theta_N) & \sin(H\theta_N) \end{bmatrix}; \; \Psi^{-1} = \frac{2}{N}\begin{bmatrix} \frac{1}{2} & \cdots & \frac{1}{2} \\ \cos(\theta_1) & \cdots & \cos(\theta_N) \\ \sin(\theta_1) & \cdots & \sin(\theta_N) \\ \vdots & & \vdots \\ \cos(H\theta_1) & \cdots & \cos(H\theta_N) \\ \sin(H\theta_1) & \cdots & \sin(H\theta_N) \end{bmatrix} \tag{30}$$

Ψ^{-1} the pseudo inverse of ψ, $N > 2H + 1$ the number of time samples and $\theta_i = \omega t_i \forall \; i = 1 \ldots N$. The analytical derivatives are more detailed in [31].

4.2. Computation of the active control force

The active control force is also written as a Fourier series

$$f_{aNL}(t) = c_0 + \sum_{k=1}^{H} c_k \cos(\omega k t) + d_k \sin(\omega k t) \tag{31}$$

whose Fourier coefficients c_k and d_k can be obtained analytically by means of an integral over a period $T = \frac{2\pi}{\omega}$ or over a period 2π if $\theta = \omega t$ is used instead of t:

$$c_k = \frac{1}{T}\int_0^T f_{aNL}(t)\cos(\omega k t)dt = \frac{1}{2\pi}\int_0^{2\pi} f_{aNL}(\theta)\cos(k\theta)dt \tag{32}$$

$$d_k = \frac{1}{T}\int_0^T f_{aNL}(t)\sin(\omega k t)dt = \frac{1}{2\pi}\int_0^{2\pi} f_{aNL}(\theta)\sin(k\theta)dt \tag{33}$$

As shown in Fig. 3, a periodic solution crosses the sliding surface at $\theta = \theta^*$ and $\theta = \theta^* + \pi$, where the active force undergoes a sign change and is therefore discontinuous. As a consequence, integrals 32 and 33 must be split in two parts from 0 to θ^* and from θ^* to $\theta^* + \pi$. Using the symmetry of f_{aNL} finally yields:

$$c_k = \frac{2}{\pi}\int_{\theta^*}^{\theta^*+\pi} f_{aNL}(\theta)\cos(k\theta)dt = \frac{4\rho}{k\pi}\sin(k\theta^*) \tag{34}$$

$$d_k = \frac{2}{\pi}\int_{\theta^*}^{\theta^*+\pi} f_{aNL}(\theta)\sin(k\theta)dt = -\frac{4\rho}{k\pi}\cos(k\theta^*) \tag{35}$$

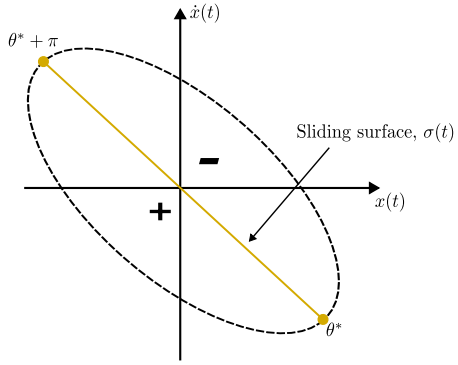

Figure 3: Phase portrait: periodic solution in dashed line and sliding surface in orange

Since θ^* corresponds to the intersection of a periodic solution with the sliding surface, it solves:

$$\sigma(\theta^*) = \sigma(\omega t^*) = 0 \tag{36}$$

and can be found with a Newton-Raphson iteration procedure (more details in algorithm 1). This technique is much more faster than the AFT method used for $f_{nl}(x, \dot{x})$ but is only possible because of the specific form of $f_{aNL}(t)$. Since $f_{aNL}(t)$ is a non-smooth function, a large number of harmonics are required to mitigate the effects of the Gibbs phenomenon, as illustrated in figure 4. Introducing a regularization of the signum function reduces the number of harmonics, but the analytical calculation of the regularized function coefficients can be complex. Consequently, a numerical integration of the Fourier coefficients is performed between the limits of θ^* and $\theta^+\pi$. Figure 5 shows the number of harmonics required to reach convergence with the regularization of the signum function by:

$$f_{aNL}(t) = \rho\frac{\sigma}{\sqrt{\sigma^2 + \epsilon}} \tag{37}$$

For the reasons given in Sect. 3.2, the term $\sqrt{\sigma}$ will be used in front of the non-linear active part (see Eq. (38)) in the following sections of this manuscript. Figure 6 shows the temporal representation of the law used. The algorithm for calculating nonlinear active forces is summarized in figure 7.

$$f_{aNL}(t) = \rho \sqrt{|\sigma|} \frac{\sigma}{\sqrt{\sigma^2 + \epsilon}} \tag{38}$$

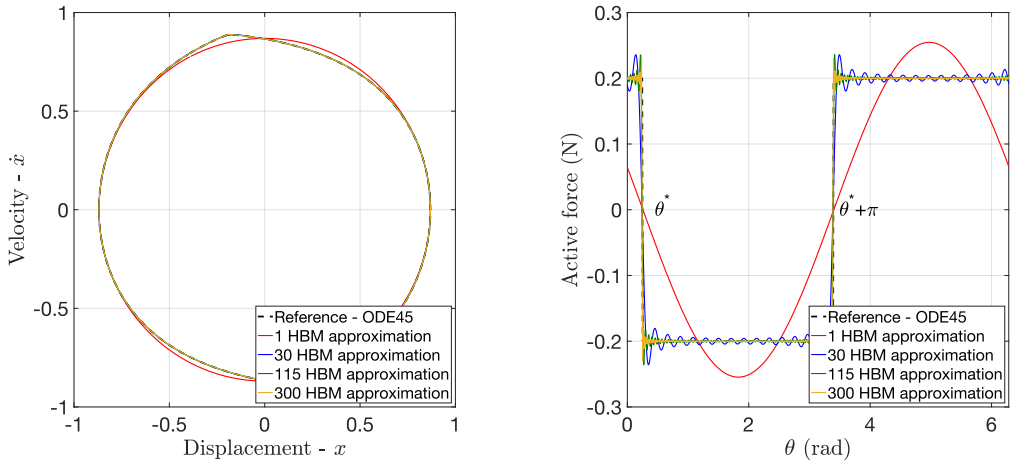

Figure 4: Non-smooth law (signum function): evolution of convergence as a function of the number of harmonics for $\rho = -0.2$: (left) Nonlinear active force, (right) Phase plan

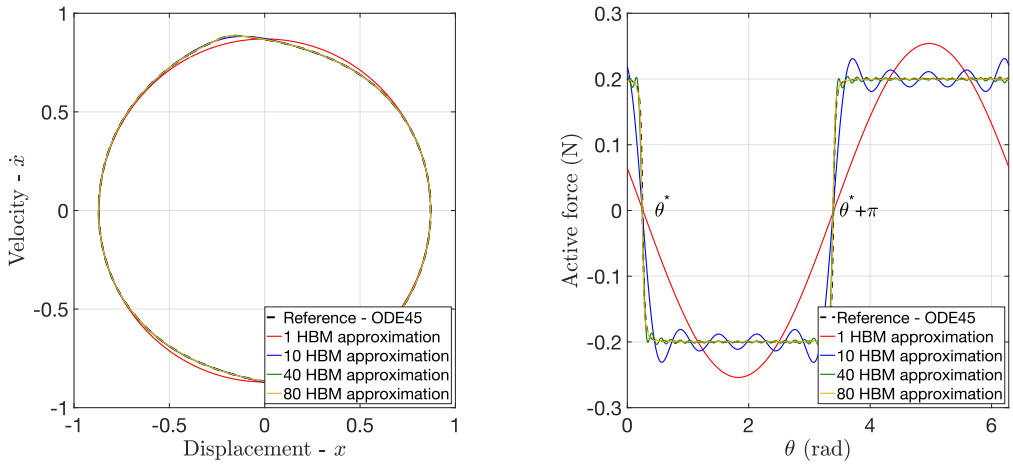

Figure 5: Smooth law as expressed in Eq.(37): evolution Regularized law: evolution of convergence as a function of the number of harmonics for $\rho = -0.2$ and $\epsilon = 10^{-2}$. (left) Nonlinear active force, (right) Phase plan

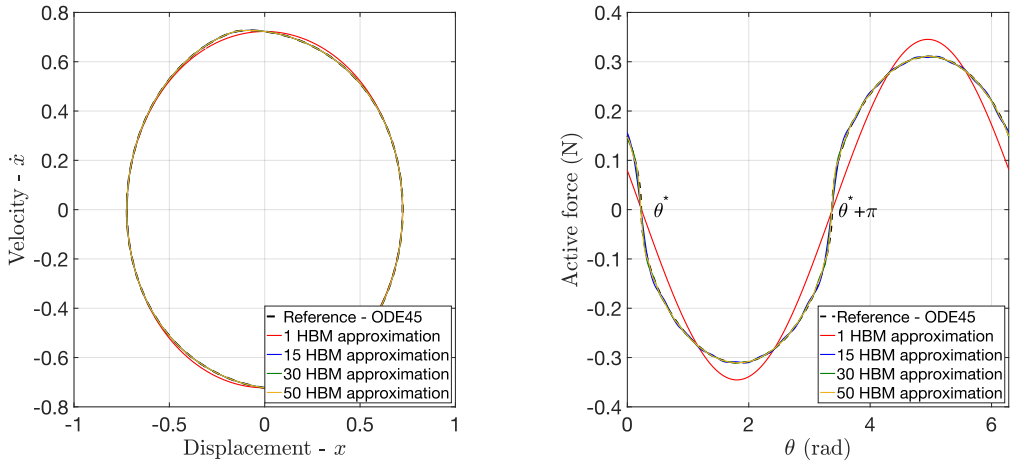

Figure 6: Smooth law as expressed in Eq.(38): evolution Regularized law: evolution of convergence as a function of the number of harmonics for $\rho = -0.2$ and $\epsilon = 10^{-5}$. (left) Nonlinear active force, (right) Phase plan

Algorithm 1 Algorithm proposed to calculate θ^*

$i \leftarrow 1$
$\theta^* \leftarrow \theta_0 = \omega t_0$
$\sigma(\theta^*) \leftarrow \alpha_1 x(t_0) + \alpha_2 \dot{x}(t_0) + \alpha_3 \int_0^{t_0} x(\tau) d\tau$
while $\|\sigma\| \leq \epsilon$ & $i \leq i_{max}$ **do**
  Compute $J = \dot{\sigma}(\theta^*) = \alpha_1 \dot{x}(t_i) + \alpha_2 \ddot{x}(t_i) + \alpha_3 x(t_i)$
  $\delta_\theta \leftarrow -J^{-1}\sigma(\theta^*)$
  $\theta^* \leftarrow \theta^* + \delta_\theta$
  $i \leftarrow i + 1$
  $\sigma(\theta^*) \leftarrow \alpha_1 x(t_{i+1}) + \alpha_2 \dot{x}(t_{i+1}) + \alpha_3 \int_0^{t_{i+1}} x(\tau) d\tau$
end while

See Algorithm 1

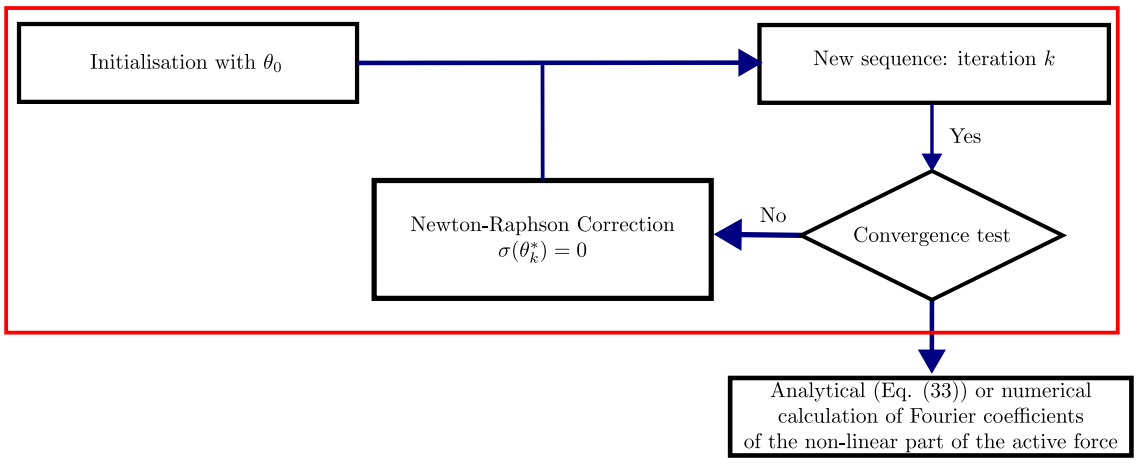

Figure 7: Algorithm: calculation of the non-linear active part.

4.3. Continuation procedure

The continuation procedure is the main tool of nonlinear dynamics. Coupled with a periodic solution algorithm (see section 3), it allows building the frequency response function (FRF). There are two main families of continuation methods. First, the asymptotic method [32, 33] based on asymptotic series expansion and the prediction-correction method such as the pseudo-arc-length used by Crisfiel, M. A in [34]. In this section, we focus on the latter method to avoid quadratic formalism.
Assuming R_X, R_Y, R_ω the Jacobian matrices of $R(X, Y, \Omega)$, such that:

$$R_X = \frac{\partial R(X,Y,\omega)}{\partial X} = Z(\omega) + \frac{dF_{nl}(X)}{dX} + \frac{\partial F_a(X,Y,\omega)}{\partial X} \tag{39}$$

$$R_Y = \frac{\partial R(X,Y,\omega)}{\partial Y} = \frac{\partial F_a(X,Y,\omega)}{\partial Y} \tag{40}$$

$$R_\omega = \frac{\partial R(X,Y,\omega)}{\partial \omega} = \frac{\partial Z(\omega)}{\partial \omega} X + \frac{\partial F_a(X,Y,\omega)}{\partial \omega} = \left[2\omega\nabla^2 M + \nabla C\right] X + \frac{\partial F_a(X,Y,\omega)}{\partial \omega} \tag{41}$$

and H_X, H_Y, H_ω the Jacobian matrices of $H(X, Y, \Omega)$, such that:

$$H_X = -\frac{1}{\omega}\tilde{\nabla} \tag{42}$$

$$H_Y = I_{2H+1} \tag{43}$$

$$H_\omega = \frac{1}{\omega^2}\tilde{\nabla} X \tag{44}$$

where $I_{2H+1} \in \mathbb{R}^{(2H+1)\times 2H+1)}$ the identity matrix. The pseudo arc length method starts with solutions (X^k, Y^k, ω^k), where k is the number of iterations. The first step is to predict an approximate solution using a tangent vector t_k

$$t_k = \left[\Delta X^T \ \Delta Y^T \ \Delta\omega\right]^T \tag{45}$$

obtained by solving

$$\begin{bmatrix} R_X & R_Y & R_\omega \\ H_X & H_Y & H_\omega \\ \Delta X^T & \Delta Y^T & \Delta\omega \end{bmatrix} \begin{bmatrix} \Delta X \\ \Delta Y \\ \Delta\omega \end{bmatrix} = \begin{bmatrix} 0_{2H+1,1} \\ 0_{2H+1,1} \\ 1 \end{bmatrix} \tag{46}$$

to make the vector t_k unitary, a normalization is added such that:

$$\Delta_s^2 = \|t_k\| = \Delta X^T \Delta X + \Delta Y^T \Delta Y + \Delta\omega^2 \tag{47}$$

The step length Δ_s is adapted according to the number of iterations of the Newton-Raphson algorithm [35]. The prediction at each iteration $k > 1$, is given by:

$$\begin{bmatrix} X_1 \\ Y_1 \\ \omega_1 \end{bmatrix} = \begin{bmatrix} X_0 \\ Y_0 \\ \omega_0 \end{bmatrix} + \begin{bmatrix} \Delta X \\ \Delta Y \\ \Delta\omega \end{bmatrix} \tag{48}$$

The second consists of successive corrections along the direction orthogonal to the tangent vector t_k using a Newton-Raphson solver. The correction at iteration k is the solution of the following solved system :

$$\begin{bmatrix} R_X^k & R_Y^k & R_\omega^k \\ H_X^k & H_Y^k & H_\omega^k \\ \Delta X^T & \Delta Y^T & \Delta\omega \end{bmatrix} \begin{bmatrix} \delta X^k \\ \delta Y^k \\ \delta\omega^k \end{bmatrix} = - \begin{bmatrix} R^k(X,Y,\omega) \\ H^k(X,Y,\omega) \\ 0 \end{bmatrix} \tag{49}$$

until the absolute value of the residual decreases to a specified tolerance level.

4.4. Stability analysis

In Section 4.3, an algorithm capable of computing the frequency response of a nonlinear system controlled by sliding mode was presented. In order to obtain all the information about the dynamics of the system, the stability of the periodic solutions is treated. This information gives the stable and unstable branches of the FRF and the associated bifurcation points. In the frequency domain, as in the work of Von Groll et al. [36], Hill's method allows transforming a time-varying problem into an eigenvalue problem. The stability of the periodic solutions follows from the study of the eigenvalues.

In this manuscript, Hill's method is modified to the integral term $Y = \frac{1}{\omega}\tilde{\nabla}X$. As we will show, the latter introduces a new variable in the system and forces the Hill problem to be singular. First of all, let us define:

$$x(t) = x_p(t) + s(t),\ y(t) = y_p(t) + r(t) \tag{50}$$

where $r(t)$, $s(t)$ are the perturbations and $y_p(t)$, $x_p(t)$ the periodic solutions. Assuming $s(t)$ and $r(t)$ such that:

$$s(t) = p(t)e^{\Lambda t},\ r(t) = q(t)e^{\Lambda t} \tag{51}$$

$$\begin{array}{cc} \dot{s}(t) = (\dot{p}(t) + p(t)\Lambda)e^{\Lambda t} & \dot{r}(t) = (\dot{q}(t) + q(t)\Lambda)e^{\Lambda t} \\ \ddot{s}(t) = (\ddot{p}(t) + 2\Lambda\dot{p}(t) + p(t)\Lambda^2)e^{\Lambda t} & \ddot{r}(t) = (\ddot{q}(t) + 2\Lambda\dot{q}(t) + q(t)\Lambda^2)e^{\Lambda t} \end{array} \tag{52}$$

with Λ being the Floquet exponents and $p(t)$, $q(t)$ the periodic solutions. Similarly, we define the non-linear and active perturbed forces:

$$\left\{\begin{array}{lcl} F_{nl}(x_p(t) + s(t)) & \approx & F_{nl}(x_p(t)) + \frac{\partial F_{nl}}{\partial x}s(t) \\ F_a(x_p(t) + s(t)) & \approx & F_a(x_p(t)) + \frac{\partial F_a}{\partial x}s(t) \\ F_a(y_r(t) + s(t)) & \approx & F_a(y_p(t)) + \frac{\partial F_a}{\partial y}r(t) \\ F_a(\dot{x}_p(t) + \dot{s}(t)) & \approx & F_a(\dot{x}_p(t)) + \frac{\partial F_a}{\partial \dot{x}}\dot{s}(t) \end{array}\right. \tag{53}$$

Following the same Galerkin procedure as Eqs.(50), (53) in the system (16) and after several mathematical manipulations, the perturbed time system is written as:

$$\left\{\begin{array}{c} M\ddot{s}(t) + (X + \frac{\partial F_a}{\partial \dot{x}})\dot{s}(t) + \left(K + \frac{\partial F_{nl}}{\partial x} + \frac{\partial F_a}{\partial x}\right)s(t) + \frac{\partial F_a}{\partial y}r(t) = 0 \\ \dot{r} = s \end{array}\right. \tag{54}$$

$$\Longrightarrow \left\{\begin{array}{c} M(\ddot{p}(t) + 2\Lambda\dot{p}(t) + p(t)\Lambda^2) + (C + \frac{\partial F_a}{\partial \dot{x}})(\dot{p}(t) + p(t)\Lambda) + \left(K + \frac{\partial F_{nl}}{\partial x} + \frac{\partial F_a}{\partial x}\right)p(t) + \frac{\partial F_a}{\partial y}q(t) = 0 \\ (\dot{q}(t) + q(t)\Lambda) = p(t) \end{array}\right. \tag{55}$$

Let ϕ and ψ be the Fourier coefficients of $p(t)$ and $q(t)$, respectively, such that

$$p(t) = T_H(\omega t)\phi,\ q(t) = T_H(\omega t)\psi \tag{56}$$

According to the procedure described in Sect.3, the frequency quadratic eigenvalue problem is given by:

$$\left\{\begin{array}{rcl} (\Lambda^2\Delta_2 + \Lambda\Delta_1 + R_X)\phi + R_Y\psi & = & 0 \\ (P_Y + \Lambda I_{2H+1})\psi & = & \phi \end{array}\right. \tag{57}$$

where

$$\left\{\begin{array}{rcc} \Delta_2 & = & I_{(2H+1)}M \\ \Delta_1 & = & 2\omega\nabla M + I_{2H+1}C + \left(\frac{dF_a(X,Y,\omega)}{dX}\right) \\ R_X & = & Z(\omega) + \left(\frac{dF_{nl}(X)}{dX}\right) + \left(\frac{dF_a(X,Y,\omega)}{dX}\right) \\ R_Y & = & \frac{\partial F_a(X,Y,\omega)}{\partial Y} \\ P_Y & = & \omega\nabla \end{array}\right. \tag{58}$$

The classical eigenvalue problem of introducing the new variable is performed: $\theta = \Lambda\phi$. The new system can then be written as follows:

$$(B_1 - \Lambda B_2)\begin{bmatrix}\theta \\ \phi \\ \psi\end{bmatrix} = \begin{bmatrix}0 \\ 0 \\ 0\end{bmatrix} \tag{59}$$

where

$$B_1 = \begin{bmatrix} \Delta_1 & R_\kappa & R_y \\ -I_{(2H+1)} & 0_{(2H+1)} & 0_{(2H+1)} \\ 0_{(2H+1)} & -I_{(2H+1)} & P_y \end{bmatrix} \tag{60}$$

$$B_2 = \begin{bmatrix} -\Delta_2 & 0_{(2H+1)} & 0_{(2H+1)} \\ 0_{(2H+1)} & -I_{(2H+1)} & 0_{(2H+1)} \\ 0_{(2H+1)} & 0_{(2H+1)} & -I_{(2H+1)} \end{bmatrix} \tag{61}$$

with $0_{(2H+1)}$, a null matrix of size $\mathbb{R}^{(2H+1)\times(2H+1)}$. The Floquet exponents are the eigenvalues of the B matrix:

$$B = B_2^{-1}B_1 = \begin{bmatrix} -\Delta_2^{-1}\Delta_1 & -\Delta_2^{-1}R_\kappa & -\Delta_2^{-1}R_y \\ I_{(2H+1)} & 0_{(2H+1)} & 0_{(2H+1)} \\ 0_{(2H+1)} & I_{(2H+1)} & -P_y \end{bmatrix} \tag{62}$$

Here B is singular due to the addition of the $y(t)$ variable and possesses a null eigenvalue. In order to assess stability, it is imperative to eliminate the null eigenvalue and consider only the two smallest eigenvalues of B.

The Floquet exponents λ_1, λ_2 are studied at each continuation step and the way they cross the imaginary axis tells us about the type of bifurcations, as shown in the following diagram:

1. Limit Point **(LP)** or Branch Point **(BP)** $\rightarrow \lambda_i = 0$: A stable or unstable periodic branch changes stability
2. Neimark-Sacker **(NS)** $\rightarrow \lambda_i = \pm i\kappa$: A stable quasi-periodic branch and a periodic branch are created
3. Period doubling **(PD)** $\rightarrow \lambda_i = \pm i\pi f$: A period-doubling branch is created

with $\kappa \in]0, \pi f[$ and f the frequency.

4.5. Bifurcation tracking for parametric analysis

Bifurcation tracking is widely used for parametric analysis. The main idea of this method is to introduce a new continuation parameter (control law parameter, nonlinear stiffness, etc.) to obtain the evolution of bifurcation points. The first step of the method consists in correctly characterizing the bifurcation points [37, 38]. To do this, an extended system for each bifurcation point is computed. Then, a variant of the continuation method presented in Sect.4.3 taking into account the new parameter applied. The method followed is detailed in the work of Xie et.al. [30]. For the sake of conciseness, it will not be explained in this paper.

4.6. Numerical validation of the proposed algorithm

In this section, the notions seen previously are tested on an adimensional system of Duffing type. Let us consider the following system:

$$m\ddot{x} + c\dot{x} + kx + k_{nl}x^3 = \Gamma \sin(\omega t) + F_a(t) \tag{63}$$

The Eq. (63) represents the general dynamics of a nonlinear system. In this example, the active force $F_a(t)$ is given by:

$$F_a(t) = -m\left(\frac{\alpha_3 x + \alpha_1 \dot{x}}{\alpha_2}\right) + \left(kx + c\dot{x} + k_{nl}x^3\right) - \rho\sqrt{|\sigma|} \times \frac{\sigma(t)}{\sqrt{\sigma^2 + \epsilon}} \tag{64}$$

Figure 8 (left) shows the performance of the linear part of the $\eta(t)$ control law. Figure 8 (right) shows the difference between the system without control, the function presented in Eq. (64) and a regularized form of the sign function by the saturation function for the parameters given by table 1. As shown in section 3.2, the sign function performs slightly better than the regularized function.

m	c	k	k_{knl}	Γ	ω	ρ	ϵ
1	0.2	1	0.4	0.5	1	-2	10^{-5}

Table 1: Parameters used for the numerical simulation.

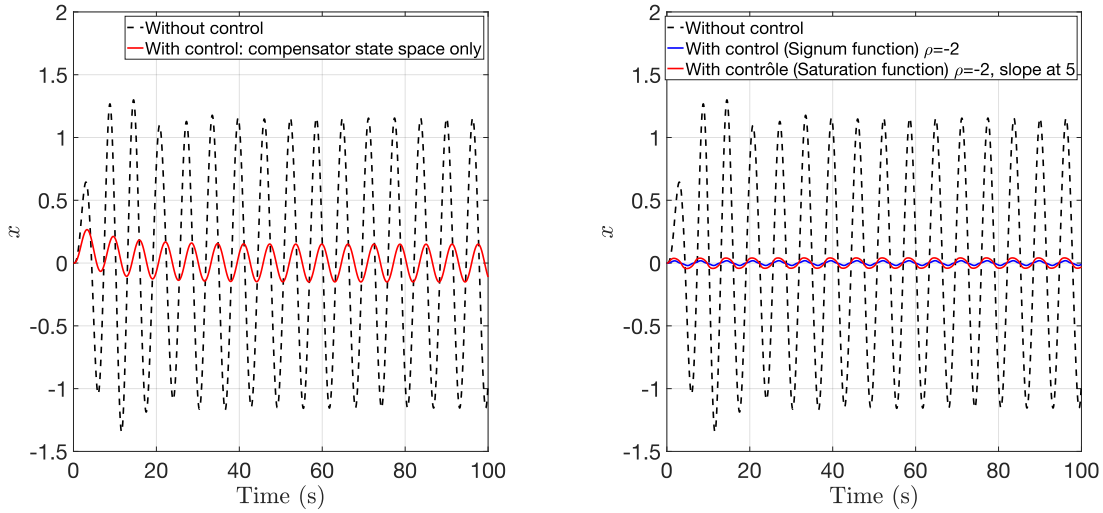

Figure 8: Temporal comparison: (left) linear active part only, (right) nonlinear and linear active part.

The parameters of the sliding surface are calculated by the linear quadratic minimization method (see section 3.1). The weighting matrix Q is chosen to be diagonal so as not to introduce state coupling in the system. Furthermore, the terms are chosen so that the performance is interesting enough to validate the proposed algorithm. The Q weighting matrices used are:

$$Q = \begin{bmatrix} 100 & 0 & 0 \\ 0 & 10 & 0 \\ 0 & 0 & 1 \end{bmatrix} \tag{65}$$

the parameters of the sliding surface $\sigma(t)$ that depend on the weighting of Q are:

$$\sigma = \begin{bmatrix} \alpha_1 = 3.261 & \alpha_2 = 1 & \alpha_3 = 0.316 \end{bmatrix} \begin{bmatrix} x_1 \\ \dot{x}_1 \\ \int x_1 \end{bmatrix} \tag{66}$$

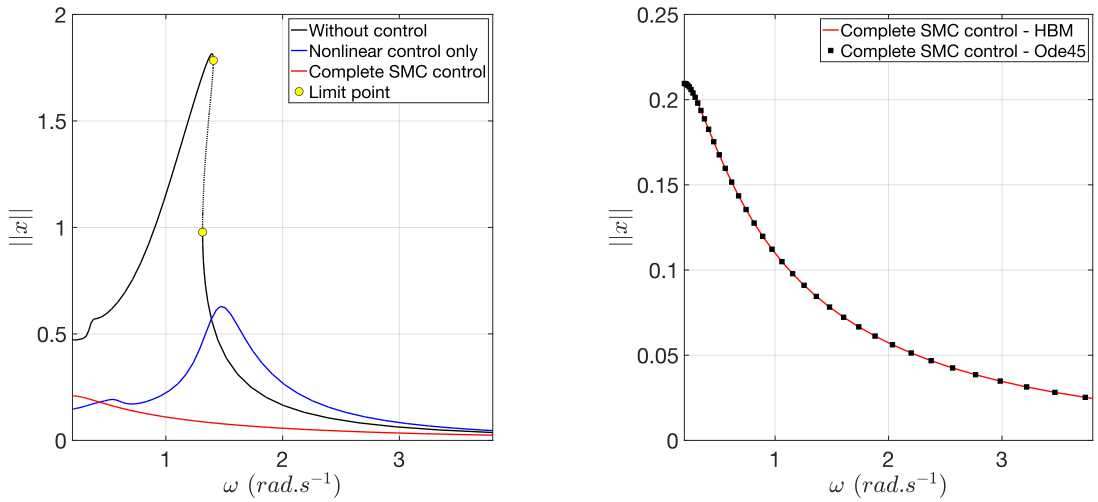

Figure 9: Frequential response - 30 Harmonics : (left) Comparison of the system without control (black), a system with nonlinear control only (blue) $\rho = 0.5$, and a system with nonlinear and linear control (red) for $\rho = 0.5$, (right). Comparison of the system calculated with the proposed algorithm (red line) and by temporal integration with ODE45 (black stars) for the system with complete active control

Fig.8 (right) shows the temporal response of the system with control without the non-linear part of the active force. It can be seen that the amplitude is already reduced compared to the system without control. However, as seen in Sect.3.1, the stability of such a controller is not guaranteed and may diverge with time. Fig.9 (left) shows the difference between the frequency response of the noncontrolled system and the controlled system with the law of Eq.(64). The system's dynamic response with active control is well-damped compared to the system without control. The coefficient $\frac{\alpha_3}{\alpha_2}$ brings a shift of the natural frequency of the controlled system induced by the continuous part of the control law. The new resonant frequency of the controlled system is given by:

$$\omega_{cont} = \sqrt{\frac{\alpha_3}{\alpha_2}} \tag{67}$$

However, The figure does not display the resonance peak due to significant damping caused by the sliding mode through the α_1 coefficient. Moreover, the controlled system does not have a static response equal to 0 at $\omega = 0 rad.s^{-1}$ due to the addition of an integral term in the control law. Figure 9 (right) shows the comparison between the system response calculated in the frequency domain and that calculated in the time domain by the Matlab ODE45 solver (with a relative tolerance accuracy of 10^{-9}). The good consistency of the proposed methods is verified.

The linear part of the linear active control $\eta(t)$ allows the theoretical linearization of the system. To obtain a true non-linear system (without the compensation of system terms), we remove this linear part. An evolution of the bifurcation point (limit point) as a function of controller gain is then presented.

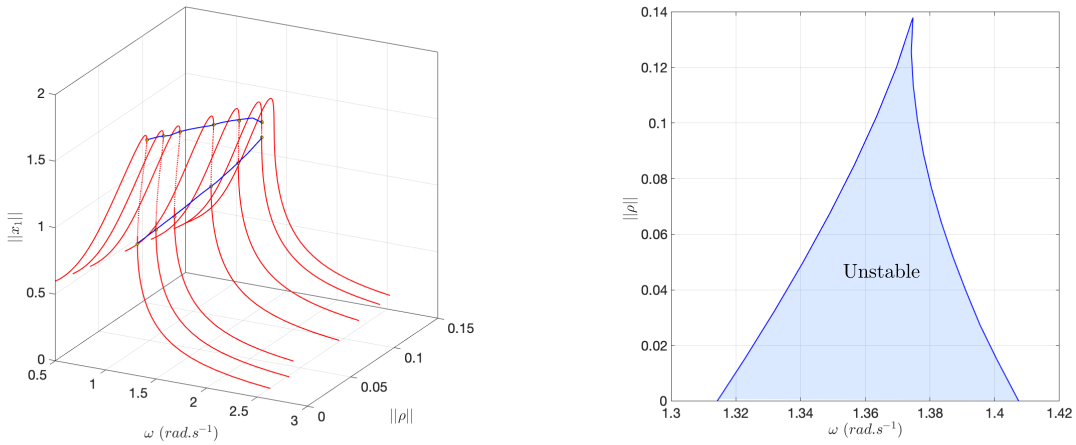

(a) (b)

Figure 10: (a)Limit point tracking with respect to the gain parameter $\sqrt{|\sigma|}\rho$ and (b) Tracking curve projection.

In Fig. 10, the branch of limit points (in blue) obtained with the bifurcation tracking algorithm (see Sect. 4.5) is plotted together with several Frequency Response Curves (FRC) to facilitate the interpretation of the results. For small values of the gain ρ, the FRC are strongly nonlinear and their unstable part is delimited by two limit points. Looking at the branch of limit points, it can be observed that the two limit points draw closer for increasing values of ρ and eventually merge for $\rho \approx 0.14$. For higher values of gain ρ, there is no longer any limit point and the FRF is linear and always stable.

5. Experimental set-up

Figure 11 depicts the system under investigation in this study. The structure is 50 cm high and 25 cm wide, and is composed of three 5mm-thick steel plates. The positioning of the electrodynamic shaker induces excitation, reaching a height of 30 cm. The mechanical arrangement of the structure, along with the positioning of the electrodynamic shaker, exhibits a slight softening behaviour. However, due to the limited stroke of the shaker, triggering this nonlinearity effectively becomes challenging. To recreate the Duffing behaviour observed and mentioned in Section 4.6, an artificial hardening nonlinearity is introduced using a control loop, following the approach employed by Abeloos et al. [39] and Zao et al. [40]. The objective is to precisely master the nonlinearity of the structure.

The measurements are performed by an accelerometer (sensitivity 9.869 pC/g) at 50cm high, a laser (sensitivity 5e-3 m/V) positioned at a height of 30 cm, and a force sensor (sensitivity 4.123 pC/N) positioned between the structure and the electrodynamic shaker, as shown in the diagram in Fig.11. The purpose of this device is to verify the experimental validity of the proposed algorithm and control design simultaneously.

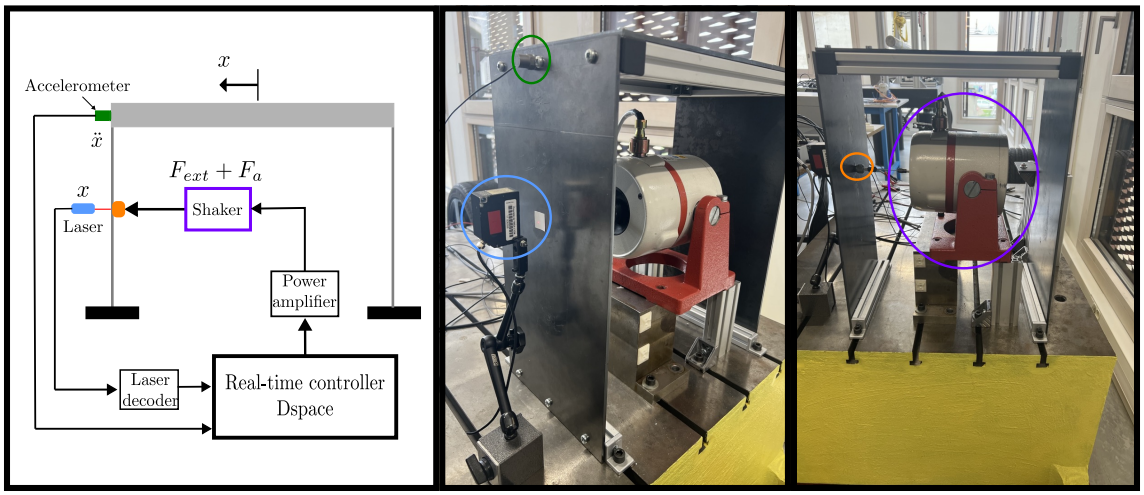

Figure 11: Experimental setup - blue circle: laser, green circle: accelerometer, orange circle: force sensor, magenta circle: electrodynamic shaker, and in yellow the seismic mass sensor.

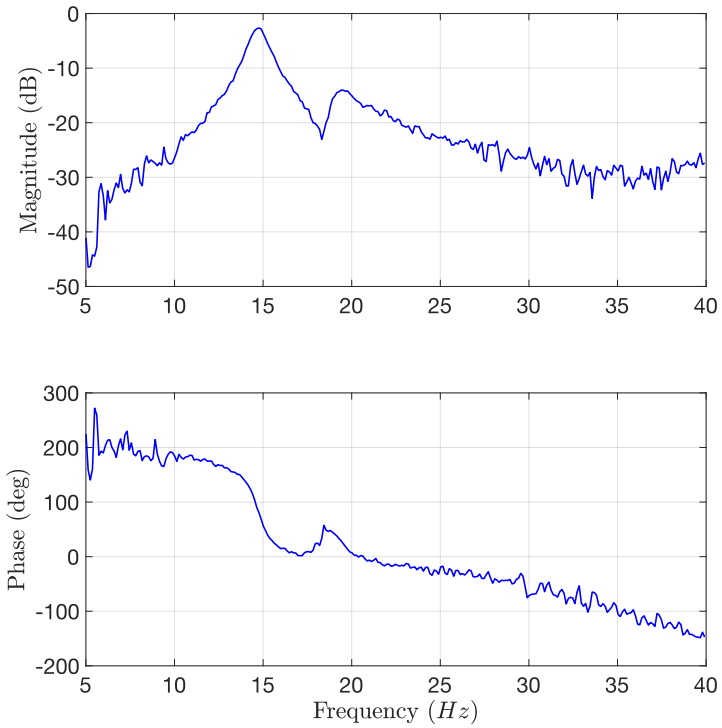

Figure 12: Bode transfer function from 5 to 40 Hz.

Figure 12 displays the frequency response function obtained using white noise, revealing the presence of the primary mode of interest at a frequency of 14.5Hz. In addition, a highly damped peak is observed around 19.4Hz, which corresponds to the pitch mode of the seismic mass. Although this peak slightly alters the phase, it has minimal impact on the cleanliness and phase characteristics of the primary mode of interest. The effective modal mass of the

structure on the first bending mode is $8.3kg$. Details of the modal mass measurement are described in Sect.5.2.

5.1. Nonlinear feedback: generation of the non-linearity

As indicated in Fig.13 a cubic stiffness is generated by nonlinear feedback based on displacement.

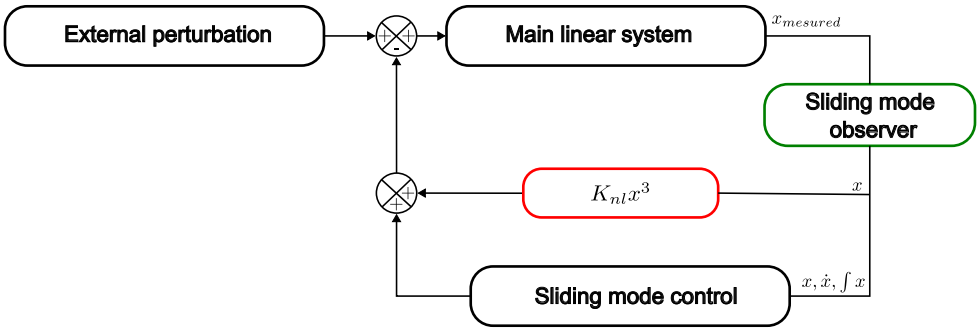

Figure 13: Block diagram: Nonlinear feedback and control on a linear structure coupled to an observer

Here, the shaker-structure interaction is not taken into account because the signal measured by the force sensor is close to the desired digital sinus [41] and the transfer function between the input voltage of the electrodynamic shaker and its output current is constant.
All the experimental data are obtained with dSpace MicroLabBox with a temporal sampling of $\Delta_t = 10^{-4}s$. The diagram shown in Fig.13 was implemented in Simulink.

5.2. System identification

In this article, the Restoring Force Surface method (RFS) method is used as in the work of Kerschen et al. [42]. The main idea of RFS is to divide the equation of motion into two parts. On the one hand inertial and external forces $m\ddot{x}$ and P, respectively, and on the other hand, a function $f(x, \dot{x})$ such that:

$$f(x, \dot{x}) = kx + knlx^3 + c\dot{x} = \lambda P - m\ddot{x} \tag{68}$$

with (k, k_{nl}, c) the modal parameters and λ the projection coefficient. The terms $\dot{x}$ and x are obtained by the numerical integration of acceleration $\ddot{x}$. The output is filtered twice by a Butterworth second-order band-pass filter with a bandwidth from 5Hz to 50Hz to suppress trends and obtain a zero-phase signal. This method is used in the work of Worden.K [43] and Keegan J. M et al. [44].

The external force is an up-and-down sinusoidal sweep [45] with an instantaneous frequency that varies from 9.5 Hz to 17.5 Hz in 100 seconds, stabilizes at 17.5 Hz for 50 seconds and then varies from 17.5 Hz to 9.5 Hz in 100 seconds, as shown in Fig.14(a). The modal mass m is found by the successive addition of a small mass δ_m on the structure. The resulting system between the modal mass, modal stiffness and appropriate pulsation (for every δ_m) is then resolved by the mean least squares method.

A least-squares fitting of $f(x, \dot{x})$ is performed to find the modal parameters (k, k_{nl}, c) and the projection coefficient λ. The resulting polynomial contains cross and non-linear terms. To know which terms are predominant in this polynomial, the I_n meaning factor is used as in the work of Worden et al. [46].

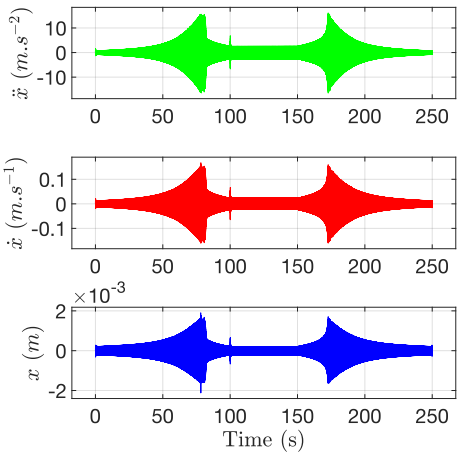

(a) Temporal accelerations and their derivatives

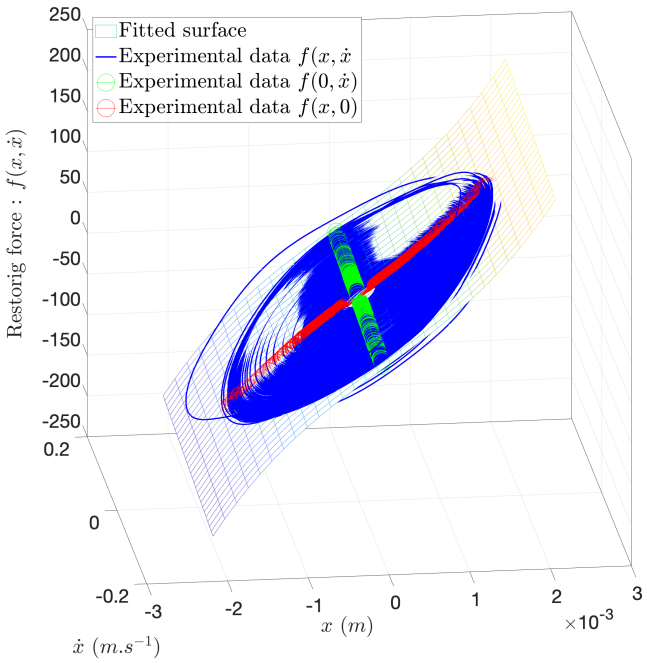

(b) Restoring force surface

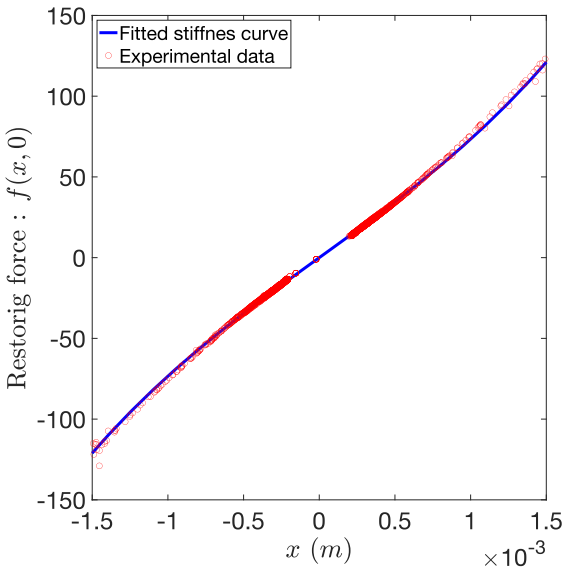

(c) Stiffness identification

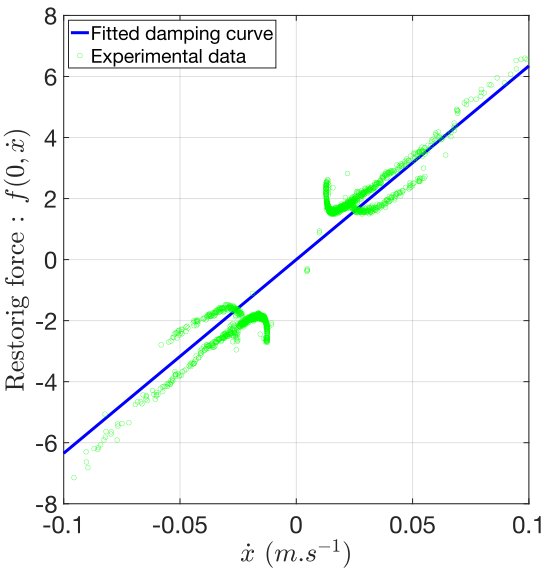

(d) Damping identification

Figure 14: Parameter identification

Damping is assumed to be linear and is manually readjusted after identification. The identified parameters and sliding surface coefficients are presented in Table 2 and 3. They will be used in the rest of the paper.

Parameters	m	c	k	k_{nl}	λ
Values	8.3 Kg	44.920 $N.s.m^{-1}$	6.753×10^4 $N.m^{-1}$	5.821×10^9 $N.m^{-3}$	0.6

Table 2: Parameters identified

Parameters	α_1	α_2	α_3
Values	27.084	8.3	2.624

Table 3: Sliding surface parameters: σ

5.3. Nonlinear sliding observer

The states of the system $(x, \dot{x}, \int xdt)$ are obtained by a "Super-Twisting Observer" [13] based on the actual displacement x_1 from the laser. The observed velocity $\hat{x}_2$ and the observed integral of the displacement $\hat{x}_3 = \int x$ is calculated by integrating the following system (69) at each time step with:

$$\begin{cases} \dot{\hat{x}}_1 = \hat{x}_2 + \lambda_1 |e_1|^{1/2} sign(e_1) \\ \dot{\hat{x}}_2 = f(x_1, \hat{x}_2, \hat{x}_3) + \lambda_2 sign(e_1) \\ \dot{\hat{x}}_3 = \hat{x}_1 \end{cases} \tag{69}$$

The coefficients λ_1 and λ_2 are determined as $\lambda_1 = 1.5L^{1/2}$ and $\lambda_2 = 1.1L$, where L represents the maximum attainable acceleration of the system [13]. These specific coefficient values are selected to strike a favourable balance between achieving rapid convergence and ensuring high accuracy [13]. $f(x_1, \hat{x}_2, \hat{x}_3)$ is the dynamical equation of the system under consideration and $e_1 = x_1 - \hat{x}_1$. A second-order elliptic high pass filter with a cutoff frequency of 2Hz was used in the last equation in order to remove DC components.

6. Experimental results and numerical comparison

In this section, the numerical and experimental results are compared. The control law used is the function (64). Excitation is provided by a sine sweep-up and sweep-down, as described in Sect. 5.2.

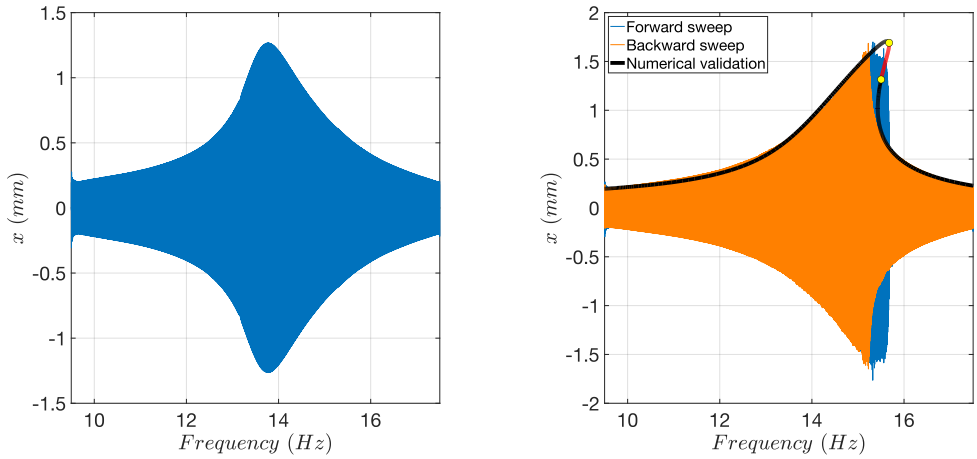

Figure 15: Experimental results - response without control: (left) Linear response without artificial nonlinearity (sweep up in blue). (right) Hardening nonlinear response (sweep up in blue and sweep down in orange). The black line, red line and yellow points indicate the numerical validation of the stable branches, the unstable branch and the limit points, respectively

Fig.15 presents the response of the structure with and without artificial nonlinearity. As mentioned in Sect.4, a slight softening nonlinearity in Fig.15 (left) is noticed. The comparison with the numerical fit model shows good consistency for the results (see Fig.15 (right)) and confirms the linear damping approximation.

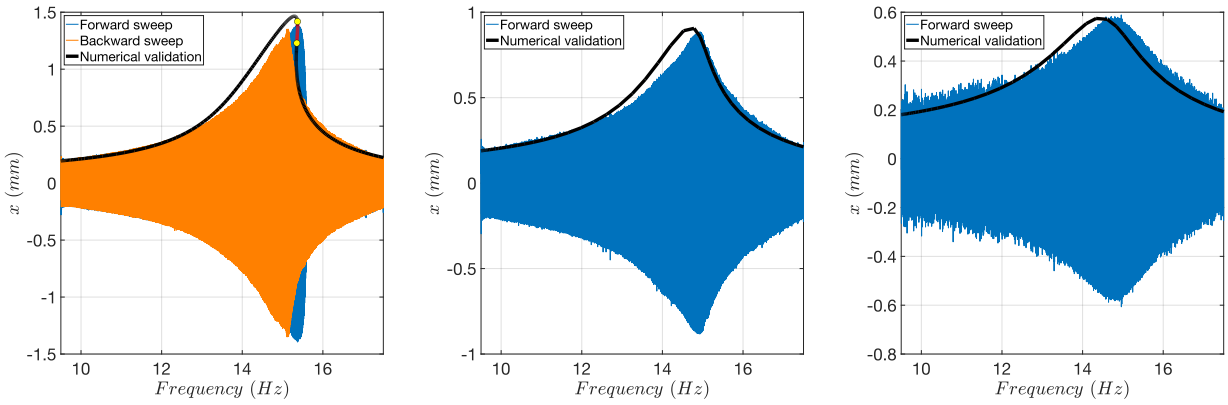

(a) $\rho = 1$ (b) $\rho = 4$ (c) $\rho = 7$

Figure 16: Experimental results - response with control (sweep up in blue and sweep down in orange), model calibration black and limit points yellow dot: (a) $\rho = 1$ and the linear part such that $0.2 \times \eta$, (b) $\rho = 4$ and the linear part such that $0.2 \times \eta$, (c) $\rho = 7$ and the linear part such that $0.2 \times \eta$.

Figure 16 shows comparison between experimental and numerical models for three values of the gain. In this study, only the gain corresponding to the non-linear part is modified. For large ρ gains, the vibratory amplitude of the structure is strongly damped. The ρ parameter serves two purposes when the system is forced. First, it improves the speed of the transient regime. The greater the value of ρ, the faster the convergence to the desired behavior. Secondly, when the limit cycle (periodic steady-state regime) is reached, it reduces the vibration amplitude. Here again, the greater the value of ρ, the greater the reduction in vibration amplitude. It is worth mentioning that this vibration damping is not due to the addition of artificial damping, but to the rejection of external disturbance caused by the non-linear part of the active force. The numerical response after adding the active control has a frequency different from the experimental one. This problem is due to the fact that the internal effects of the shaker, the power amplifier and the delay in the feedback loop are not taken into account. A more accurate identification could have been done, but it is not necessary here. The experimental results show that the prediction made by the bifurcation tracking in Fig.10 is verified. The nonlinear response becomes progressively linear as the nonlinear control effort increases. We observe experimentally the disappearance of the limit points, despite the addition of the linear part of the control. Indeed, the amplitude of the system controlled is so small that nonlinearity does not occur. To conclude this section, the proposed algorithm allows predicting the behaviour of a nonlinear structure controlled by a sliding mode control law quite accurately.

7. Conclusion

This study focused on a sliding-mode control law that incorporates a nonsmooth nonlinearity and a variable related to the integral of displacement, which poses challenges in calculating the frequency response. The article presented the development of an algorithm to calculate the frequency response of a sliding-mode controlled structure, along with a stability analysis. These two tools enabled more comprehensive understanding of the system's dynamics. To validate the proposed algorithm, an experimental one-degree-of-freedom system with localized artificial nonlinearity was devised, and the model was calibrated. This work served as the primary contribution of the paper. The results demonstrated a strong correlation between the numerical and experimental models, confirming the effectiveness of sliding mode control for systems with nonlinear dynamics. Future research will aim to extend the algorithm to two-degree-of-freedom nonlinear systems and consider the quasi-periodic nature often observed in such systems, resulting

from linearization caused by the control law. In addition, exploring the design of the control law is another avenue for investigation. The current sliding surface parameters were designed based on Hurwitz's criterion for linear systems, but it would be interesting to account for the nonlinearity of the system and solve the Riccati equation for nonlinear systems to determine these parameters. Lastly, the question of optimizing the control law arises. Potential avenues for exploration include variable gain as a function of frequency and the incorporation of artificial intelligence, as suggested in the literature [47]. These future optimizations, based on passivity, are aimed at enhancing the controller's performance in terms of energy efficiency and damping across a wide frequency range in the system studied.

References

[1] T. Krysinski, F. Malburet, Mechanical Vibrations: Active and Passive Contol, ISTE, 2007.

[2] TrelleborgVibracoustics, Automotive Vibration Control Technology: Fundamentals, Materials, Construction, Simulation, and Applications, 1st Edition, Vogel Business Media GmbH & Co. KG, 2015.

[3] S. M. Hashemi, M. F. Golnaraghi, A. E. Patla, Tuned vibration absorber for suppression of rest tremor in parkinson's disease, Medical & Biological Engineering & Computing 42 (1) (2004) 61–70. doi:10.1007/bf02351012.
URL http://link.springer.com/10.1007/BF02351012

[4] M. G. Soto, H. Adeli, Tuned mass dampers, Archives of Computational Methods in Engineering 20 (4) (2013) 419–431. doi:10.1007/s11831-013-9091-7.
URL http://link.springer.com/10.1007/s11831-013-9091-7

[5] K. Jaboviste, E. Sadoulet-Reboul, O. Sauvage, G. Chevallier, A Framework for the Design of Rotating Multiple Tuned Mass Damper, in: B. Dilworth, M. Mains (Eds.), Topics in Modal Analysis & Testing, Volume 8, Conference Proceedings of the Society for Experimental Mechanics Series, Springer International Publishing, 2021, pp. 393–397. doi:10.1007/978-3-030-47717-2_40.

[6] T. Detroux, G. Habib, L. Masset, G. Kerschen, Performance, robustness and sensitivity analysis of the nonlinear tuned vibration absorber, Mechanical Systems and Signal Processing 60 (2015) 799–809.

[7] A. H. Nayfeh, D. T. Mook, Nonlinear oscillations, John Wiley & Sons, 2008.

[8] A. Preumont, Vibration control of active structures: an introduction, Vol. 246, Springer, 2018.

[9] S. Chesné, Hybrid skyhook mass damper, Mechanics & Industry 22 (2021) 49. doi:10.1051/meca/2021050.
URL https://www.mechanics-industry.org/10.1051/meca/2021050

[10] C. Collette, S. Chesné, Robust hybrid mass damper, Journal of Sound and Vibration 375 (2016) 19–27. doi:10.1016/j.jsv.2016.04.030.
URL https://linkinghub.elsevier.com/retrieve/pii/S0022460X16300839

[11] V. Utkin, Variable structure systems with sliding modes, IEEE Transactions on Automatic Control 22 (2) (1977) 212–222. doi:10.1109/tac.1977.1101446.
URL http://ieeexplore.ieee.org/document/1101446/

[12] V. I. Utkin, Sliding Modes in Control and Optimization, Springer Berlin Heidelberg, 1992. doi:10.1007/978-3-642-84379-2.
URL http://link.springer.com/10.1007/978-3-642-84379-2

[13] Y. Shtessel, C. Edwards, L. Fridman, A. Levant, et al., Sliding mode control and observation, Vol. 10, Springer, 2014.

[14] L. Zuo, J.-J. E. Slotine, Robust vibration isolation via frequency-shaped sliding control and modal decomposition, Journal of Sound and Vibration 285 (4-5) (2005) 1123–1149. doi:10.1016/j.jsv.2004.09.014.
URL https://www.sciencedirect.com/science/article/pii/S0022460X04007588

[15] J. Rodriguez, M. Collet, S. Chesné, Active vibration control on a smart composite structure using modal-shaped sliding mode control, Journal of Vibration and Acoustics 144 (2). doi:10.1115/1.4053358.
URL https://doi.org/10.1115/1.4053358

[16] C. Kim, P. I. Ro, A sliding mode controller for vehicle active suspension systems with non-linearities, Proceedings of the Institution of Mechanical Engineers, Part D: Journal of Automobile Engineering 212 (2) (1998) 79–92. doi:10.1243/0954407981525812.
URL http://journals.sagepub.com/doi/10.1243/0954407981525812

[17] L. A. Tuan, S.-G. Lee, Sliding mode controls of double-pendulum crane systems, Journal of Mechanical Science and Technology 27 (6) (2013) 1863–1873. doi:10.1007/s12206-013-0437-8.

[18] M. Krack, J. Gross, Harmonic Balance for Nonlinear Vibration Problems, Springer International Publishing, 2019. doi:10.1007/978-3-030-14023-6.

[19] K. Nonaka, H. Sugizaki, Integral sliding mode altitude control for a small model helicopter with ground effect compensationdoi:10.1109/acc.2011.5991016.

[20] B. Sumantri, N. Uchiyama, S. Sano, Least square based sliding mode control for a quad-rotor helicopter and energy saving by chattering reduction, Mechanical Systems and Signal Processing 66-67 (2016) 769–784. doi:10.1016/j.ymssp.2015.05.013.
URL https://www.sciencedirect.com/science/article/pii/S0888327015002344

[21] j. Kautsky, n. k. Nichols, p. Van Dooren, Robust pole assignment in linear state feedback, International Journal of Control 41 (5) (1985) 1129–1155, zSCC: 0001343. doi:10.1080/0020718508961188.
URL https://doi.org/10.1080/0020718508961188

[22] S. Tokat, M. S. Fadali, O. Eray, A classification and overview of sliding mode controller sliding surface design methods, Recent Advances in Sliding Modes: From Control to Intelligent Mechatronics (2015) 417–439.

[23] J.-J. E. Slotine, W. Li, et al., Applied nonlinear control, Vol. 199, Prentice hall Englewood Cliffs, NJ, 1991.

[24] H. Lee, V. I. Utkin, Chattering suppression methods in sliding mode control systems, Annual Reviews in Control 31 (2) (2007) 179–188. doi:10.1016/j.arcontrol.2007.08.001.
URL https://www.sciencedirect.com/science/article/pii/S1367578807000363

[25] H. Dankowicz, F. Schilder, Recipes for continuation, SIAM, 2013.

[26] L. Renson, G. Kerschen, B. Cochelin, Numerical computation of nonlinear normal modes in mechanical engineering, Journal of Sound and Vibration 364 (2016) 177–206. doi:10.1016/j.jsv.2015.09.033.
URL https://linkinghub.elsevier.com/retrieve/pii/S0022460X15007543

[27] A. H. Nayfeh, B. Balachandran, Applied Nonlinear Dynamics: Analytical, Computational, and Experimental Methods, John Wiley & Sons, 2008. arXiv:E2GckXZPYegC.

[28] M. Urabe, Galerkin's procedure for nonlinear periodic systems, Archive for Rational Mechanics and Analysis 20 (2) (1965) 120–152. doi:10.1007/bf00284614.
URL https://doi.org/10.1007/BF00284614

[29] T. M. Cameron, J. H. Griffin, An alternating frequency/time domain method for calculating the steady-state response of nonlinear dynamic systems, Journal of Applied Mechanics 56 (1) (1989) 149–154. doi:10.1115/1.3176036.
URL https://doi.org/10.1115/1.3176036

[30] L. Xie, S. Baguet, B. Prabel, R. Dufour, Bifurcation tracking by harmonic balance method for performance tuning of nonlinear dynamical systems, Mechanical Systems and Signal Processing 88 (2017) 445–461. doi:10.1016/j.ymssp.2016.09.037.
URL https://linkinghub.elsevier.com/retrieve/pii/S0888327016303843

[31] M. Krack, L. P. von Scheidt, J. Wallaschek, A high-order harmonic balance method for systems with distinct states, Journal of Sound and Vibration 332 (21) (2013) 5476–5488. doi:10.1016/j.jsv.2013.04.048.
URL https://linkinghub.elsevier.com/retrieve/pii/S0022460X13004057

[32] B. Cochelin, C. Vergez, A high order purely frequency-based harmonic balance formulation for continuation of periodic solutions, Journal of Sound and Vibration 324 (1-2) (2009) 243–262. doi:10.1016/j.jsv.2009.01.054.
URL https://hal.archives-ouvertes.fr/hal-00315288

[33] N. Damil, M. Potier-Ferry, A new method to compute perturbed bifurcations: Application to the buckling of imperfect elastic structures, International Journal of Engineering Science 28 (9) (1990) 943–957. doi:10.1016/0020-7225(90)90043-i.
URL https://www.sciencedirect.com/science/article/pii/002072259090043I

[34] M. Crisfield, A fast incremental/iterative solution procedure that handles "snap-through", Computers & Structures 13 (1-3) (1981) 55–62. doi:10.1016/0045-7949(81)90108-5.
URL https://www.sciencedirect.com/science/article/pii/0045794981901085

[35] R. Seydel, Practical Bifurcation and Stability Analysis, Springer Science & Business Media, 2009. arXiv:4Xvr1xzaCZEC.

[36] G. V. Groll, D. Ewins, The harmonic balance method with arc-length continuation in rotor/stator contact problems, Journal of Sound and Vibration 241 (2) (2001) 223–233. doi:10.1006/jsvi.2000.3298.
URL https://www.sciencedirect.com/science/article/pii/S0022460X0093298X

[37] E. P. Petrov, Analysis of bifurcations in multiharmonic analysis of nonlinear forced vibrations of gas-turbine engine structures with friction and gaps (2015) 14.

[38] R. Alcorta, S. Baguet, B. Prabel, P. Piteau, G. Jacquet-Richardet, Period doubling bifurcation analysis and isolated sub-harmonic resonances in an oscillator with asymmetric clearances, Nonlinear Dynamics 98 (4) (2019) 2939–2960. doi:10.1007/s11071-019-05245-6.
URL http://link.springer.com/10.1007/s11071-019-05245-6

[39] G. Abeloos, L. Renson, C. Collette, G. Kerschen, Stepped and swept control-based continuation using adaptive filtering, Nonlinear Dynamics 104 (4) (2021) 3793–3808. doi:10.1007/s11071-021-06506-z.
URL https://doi.org/10.1007/s11071-021-06506-z

[40] G. Zhao, A. Paknejad, G. Raze, A. Deraemaeker, G. Kerschen, C. Collette, Nonlinear positive position feedback control for mitigation of nonlinear vibrations, Mechanical Systems and Signal Processing 132 (2019) 457–470. doi:10.1016/j.ymssp.2019.07.005.
URL https://www.sciencedirect.com/science/article/pii/S0888327019304339

[41] G. Abeloos, F. Müller, E. Ferhatoglu, M. Scheel, C. Collette, G. Kerschen, M. Brake, P. Tiso, L. Renson, M. Krack, A consistency analysis of phase-locked-loop testing and control-based continuation for a geometrically nonlinear frictional system, Mechanical Systems and Signal Processing 170 (2022) 108820. doi:10.1016/j.ymssp.2022.108820.
URL https://linkinghub.elsevier.com/retrieve/pii/S0888327022000188

[42] G. Kerschen, K. Worden, A. F. Vakakis, J.-C. Golinval, Past, present and future of nonlinear system identification in structural dynamics, Mechanical Systems and Signal Processing 20 (3) (2006) 505–592. doi:10.1016/j.ymssp.2005.04.008.
URL https://www.sciencedirect.com/science/article/pii/S0888327005000828

[43] K. Worden, Data processing and experiment design for the restoring force surface method, part II: Choice of excitation signal, Mechanical Systems and Signal Processing 4 (4) (1990) 321–344. doi:10.1016/0888-3270(90)90011-9.
URL https://www.sciencedirect.com/science/article/pii/0888327090900119

[44] K. J. Moore, M. Kurt, M. Eriten, D. M. McFarland, L. A. Bergman, A. F. Vakakis, Time-series-based nonlinear system identification of strongly nonlinear attachments, Journal of Sound and Vibration 438 (2019) 13–32. doi:10.1016/j.jsv.2018.09.033.
URL https://linkinghub.elsevier.com/retrieve/pii/S0022460X18306187

[45] K. Worden, Data processing and experiment design for the restoring force surface method, part i: integration and differentiation of measured time data, Mechanical Systems and Signal Processing 4 (4) (1990) 295–319. doi:10.1016/0888-3270(90)90010-i.

[46] K. Worden, G. R. Tomlinson, Nonlinearity in Structural Dynamics, CRC Press, 2019. doi:10.1201/9780429138331.

[47] J. Fu, F. Huang, Z. Chen, Optimization-based adaptive neural sliding mode control for nonlinear systems with fast and accurate response under state and input constraints, Journal of the Franklin Institute 359 (13) (2022) 6735–6758. doi:10.1016/j.jfranklin.2022.07.010.
URL https://www.sciencedirect.com/science/article/pii/S0016003222004653